V European Conference on Computational Fluid Dynamics
ECCOMAS CFD 2010
J. C. F. Pereira and A. Sequeira (Eds)
Lisbon, Portugal, 14–17 June 2010

LES MODELING OF COMBUSTION APPLICATIONS USING OpenFOAM

M. Chapuis, C. Fureby, E. Fedina, N. Alin & J. Tegnér
Defense Security Systems Technology, The Swedish Defense Research Agency – FOI,
SE 147 25 Tumba, Stockholm, Sweden
fureby@foi.se (corresponding author)

Key words. LES, Reacting Flows, OpenFoam, Gas Turbines, Ram- and scramjet

Abstract. *Predictive modeling of turbulent combustion is important for the development of IC engines, air-breathing engines, furnaces and for the understanding of afterburning behind explosive blasts. Significant advances in modeling non-reactive turbulent flows are now possible with the development of Large Eddy Simulation (LES) in which the large energetic scales of the flow are resolved on the grid whilst modeling the effects of the small scales. Here we discuss the use of combustion LES in predictive modeling of propulsion and afterburning behind explosive blasts. The LES models used are described in some detail and are validated against laboratory data – of which results from two cases are presented. These validated LES models are then applied to an annular multi-burner gas turbine combustor, a simplified scramjet combustor and condensed phase explosive TNT air blast, for which some additional experimental data is available. For these cases good agreement with the available reference data is obtained, and the LES predictions are used to elucidate the flow physics in such devices to further enhance our knowledge of these propulsion systems. Particular attention is focused on the influence of the combustion chemistry, turbulence-chemistry interaction, self-ignition, flameholding burner-to-burner interactions and combustion oscillations and instabilities.*

1. INTRODUCTION

Predictive modeling of turbulent combustion is becoming increasingly important for the development of air-breathing engines, combustion engines, furnaces and for understanding afterburning behind explosive blasts. The increase in computational power in the past decade has made some of these flow configurations numerically accessible. Nevertheless, the interaction of turbulence with physical processes, such as chemical kinetics and thermal radiation is a great challenge. In the gas turbine industry, Reynolds Averaged Navier Stokes (RANS) models together with flamelet or eddy break-up combustion models, [1], is the primary means of analyzing combusting flows, mainly due to its fast turnaround time and success in providing design guidance for meeting exit temperature profile requirements. RANS has also been used to predict emissions, but such predictions have met with mixed success. For high-speed ram- and scramjet engines similar methods are currently used but often together with more detailed chemical reaction mechanisms, [2], in order to better predict the ignition delay time of the mixture. A key issue for the successful operation of such engines is rapid mixing between fuel and air prior to self-ignition, which however is difficult to predict with RANS. Research in condense phase explosions involve high pressures and temperatures, phase transitions, turbulence, shocks, mixing, instabilities, chemical reactions and deflagration-to-detonation transition, putting significant demands on the simulation methodology, [3]. Significant advances in modeling non-reactive turbulent flows are now possible with the development of Large Eddy Simulation (LES), [4-5]. The philosophy behind LES is to explicitly solve for the large (energetic) scale flow, directly affected by boundary conditions, and model the small (less energetic) scale flow. The development of LES have so far primarily been based on ordinary turbulence theory and on RANS, [6], resulting in improved predictions due mainly to that in LES the large scales are resolved. Considering the use of LES for combustion we recognize the benefits offered by resolving the large scale flow, but need to develop better understanding for what is required in terms of modeling the turbulence chemistry interactions, in particular for reduced or global reaction mechanisms, and how well such simulations can predict mixing, self-ignition, flame-stabilization, combustion oscillations in complex geometries.

The objective of this paper is to discuss the current state of the art in computational combustion using OpenFOAM. Here we present the LES combustion model, the numerical methods used to solve the governing equations and show results for two validation cases for which high-quality experimental data is used to benchmark the accuracy of the combustion LES model. In addition, we also present results from a multi-burner annular aero gas turbine simulation, a scramjet combustor simulation and a simulation of afterburning behind an expanding shock wave of a condensed phase explosion to illustrate the versatility, robustness and usefulness of the OpenFOAM-based combustion model.

2. LARGE EDDY SIMULATION COMBUSTION MODELING

The reactive flow equations are the balance equations of mass, momentum and energy describing convection, diffusion and reactions, [7]. In LES, these are filtered, [4], to remove

the dependence on the small eddy scales, resulting in the LES equations,

$$\begin{cases} \partial_t(\overline{\rho})+\nabla\cdot(\overline{\rho}\tilde{\mathbf{v}})=0, \\ \partial_t(\overline{\rho}\tilde{Y}_i)+\nabla\cdot(\overline{\rho}\tilde{\mathbf{v}}\tilde{Y}_i)=\nabla\cdot(\overline{\mathbf{j}_i}-\mathbf{b}_i)+\overline{\dot{w}_i}, \\ \partial_t(\overline{\rho}\tilde{\mathbf{v}})+\nabla\cdot(\overline{\rho}\tilde{\mathbf{v}}\otimes\tilde{\mathbf{v}})=-\nabla\overline{p}+\nabla\cdot(\overline{\mathbf{S}}-\mathbf{B}), \\ \partial_t(\overline{\rho}\tilde{E})+\nabla\cdot(\overline{\rho}\tilde{\mathbf{v}}\tilde{E})=\nabla\cdot(-\overline{p}\tilde{\mathbf{v}}+\tilde{\mathbf{S}}\tilde{\mathbf{v}}+\overline{\mathbf{h}}-\mathbf{b}_E), \end{cases} \tag{1}$$

in which $^-$ and $^\sim$ denotes filtered and Favré filtered quantities, respectively. In addition, ρ is the density, $\mathbf{v}$ the velocity, p the pressure, $\mathbf{S}$ the viscous stress tensor, $E=h-p/\rho+\frac{1}{2}\mathbf{v}^2$ the energy, h the enthalpy, $\mathbf{h}$ the heat flux vector, and Y_i, $\mathbf{j}_i$ and $\dot{w}_i$ the mass fraction, mass diffusion and reaction rate of specie i, where the subgrid physics is hidden in the unresolved transport (or subgrid) terms $\mathbf{B}=\overline{\rho}(\widetilde{\mathbf{v}\otimes\mathbf{v}}-\tilde{\mathbf{v}}\otimes\tilde{\mathbf{v}})$, $\mathbf{b}_i=\overline{\rho}(\widetilde{\mathbf{v}Y_i}-\tilde{\mathbf{v}}\tilde{Y}_i)$ and $\mathbf{b}_E=\overline{\rho}(\widetilde{\mathbf{v}E}-\tilde{\mathbf{v}}\tilde{E})$, e.g. [8]. Based on [9] we assume the gas mixture to be linearly viscous, with Fourier heat conduction and Fickian diffusion, and by ignoring the subgrid parts of the constitutive equations, $\overline{\mathbf{S}}\approx 2\mu\tilde{\mathbf{D}}_D$, $\overline{\mathbf{h}}\approx\kappa\nabla\tilde{T}$, $\overline{\mathbf{j}_i}\approx D_i\nabla\tilde{Y}_i$ and $\overline{p}\approx\overline{\rho}R\tilde{T}\Sigma_i(\tilde{Y}_i/M_i)$, in which $\tilde{\mathbf{D}}_D$ is the deviatoric part of $\tilde{\mathbf{D}}=\frac{1}{2}(\nabla\tilde{\mathbf{v}}+\nabla\tilde{\mathbf{v}}^T)$, $\tilde{T}$ the temperature and R the gas constant. The viscosity, μ, is modeled by Sutherland's law and the species and thermal diffusivities are $D_i=\mu/Sc_i$ and $\kappa=\mu/Pr$, respectively, where Sc_i and Pr are the Schmidt and Prandtl numbers. Filtering of the energy variable results in that $\tilde{E}=\tilde{h}-\overline{p}/\overline{\rho}+\frac{1}{2}\tilde{\mathbf{v}}^2+k$, in which $k=\frac{1}{2}(\widetilde{\mathbf{v}^2}-\tilde{\mathbf{v}}^2)$ is the subgrid kinetic energy and $\tilde{h}=\Sigma_i(\tilde{Y}_i h^\theta_{i,f})+\Sigma_i(\tilde{Y}_i\int_{T_0}^{\tilde{T}}C_{p,i}(T)dT)$ from which $\tilde{T}$ results. Finally, for a reaction mechanism $\Sigma_{i=1}^N P'_{ij}\mathfrak{R}_i \overset{k_{f,j}}{\underset{k_{b,j}}{\rightleftharpoons}} \Sigma_{i=1}^N P''_{ij}\mathfrak{R}_i$, where k_{fj} and k_{bj} are the forward and backward Ahrrenius reaction rate constants, respectively, the filtered species reactions rates are $\overline{\dot{w}_i}=M_i(P''_{ij}-P'_{ij})\overline{\dot{w}_j}$ in which the j^{th} reaction rate is $\dot{w}_j=k_{f,j}\Pi_{i=1}^N(\rho Y_i)^{P'_{ij}}-k_{b,j}\Pi_{i=1}^N(\rho Y_i)^{P''_{ij}}$.

The choice of *subgrid flow model*, i.e. the modeling of $\mathbf{B}$, $\mathbf{b}_i$ and $\mathbf{b}_E$, appears not to be critical for the outcome of most LES, [10-11], whereas the *subgrid combustion model*, i.e. the overall treatment of the flame, including the modeling of the filtered reaction rates, $\overline{\dot{w}_i}$, is more important due to the interactions between the flame and flow. Concerning $\mathbf{B}$, $\mathbf{b}_i$ and $\mathbf{b}_E$ we notice that these terms are not unique to reactive flows and thus acquire models from the plethora of subgrid models for non-reactive flows, [4]. In this paper, we mainly use the Mixed Model (MM), [12-13], in which $\mathbf{B}=\overline{\rho}(\widetilde{\tilde{\mathbf{v}}\otimes\mathbf{v}}-\tilde{\tilde{\mathbf{v}}}\otimes\tilde{\mathbf{v}})-2\mu_k\tilde{\mathbf{D}}_D$, $\mathbf{b}_i=\overline{\rho}(\widetilde{\tilde{\mathbf{v}}Y_i}-\tilde{\tilde{\mathbf{v}}}\tilde{Y}_i)-\frac{\mu_k}{Sc_t}\nabla\tilde{Y}_i$ and $\mathbf{b}_E=\overline{\rho}(\widetilde{\tilde{\mathbf{v}}E}-\tilde{\tilde{\mathbf{v}}}\tilde{E})-\frac{\mu_k}{Pr_t}\nabla\tilde{E}$, with the subgrid viscosity, $\mu=\overline{\rho}c_k\Delta k^{1/2}$, being obtained from solving a modeled transport equation for the subgrid kinetic energy, k, [14], and where Sc_t and Pr_t are the turbulent Schmidt and Prandtl numbers. To reduce the computational cost we also use *wall-modeled* LES, in which a model is used to handle the near-wall flow physics, [15]. Concerning the choice of subgrid combustion model the situation is very different: From the plethora of models available we may distinguish between *flamelet models*, [16-19], in which the flame is considered thin compared to the length scales of the flow, and is hence an interface between fuel and oxidizer (for non-premixed combustion) or between reactants and products (for premixed combustion) and *finite rate chemistry models*, [20-23], which are based on modeling $\overline{\dot{w}_i}$ without specifically taking into account the intrinsic properties of the flame. The modeling of $\overline{\dot{w}_i}$ is not without problems due to the non-linear

nature of $\dot{w}_i(\rho,Y_k,T)$ and a complicating factor is that a reaction mechanism also has to be provided. However, this approach can be used to simulate both premixed and non-premixed combustion with a higher level of explicitly resolved physics.

The Thickened Flame Model (TFM) is based on the observation, [24], that the laminar flame speed, $s_u^0 \propto \sqrt{D\dot{w}/\rho^2}$, and the flame thickness, $\delta_u \propto D/\overline{\rho}/s_u^0$, where D and $\dot{w}$ are the diffusivity and reaction rate, respectively, can be used to rescale δ_u preserving s_u^0. For LES this can be realized by reducing $\dot{w}$ by a factor F, and increasing D by F so that,

$$\partial_t(\overline{\rho}\tilde{Y}_i)+\nabla\cdot(\overline{\rho}\tilde{\mathbf{v}}\tilde{Y}_i)=\nabla\cdot(FD_i\nabla\tilde{Y}_i)+F^{-1}M_iP_{ij}\dot{w}_j(\overline{\rho},\tilde{Y}_k,\tilde{T}). \quad (2)$$

The wrinkling of the thickened flame is underestimated by a factor of $E=\Xi(\delta_u)/\Xi(\delta_u^F)$, where Ξ is the wrinkling factor and δ_u^F is the resolved flame thickness. Following Colin *et al*, [20], this can be remedied by increasing the flame speed by a factor E since $s_t^0=Es_u^0$, which implies that both D and $\dot{w}$ should be multiplied with the factor E so that,

$$\partial_t(\overline{\rho}\tilde{Y}_i)+\nabla\cdot(\overline{\rho}\tilde{\mathbf{v}}\tilde{Y}_i)=\nabla\cdot(D_i\nabla\tilde{Y}_i-(1-FE)D_i\nabla\tilde{Y}_i)+EF^{-1}M_iP_{ij}\dot{w}_j(\overline{\rho},\tilde{Y}_k,\tilde{T}). \quad (3)$$

For the purpose of this study we use the fractal flame wrinkling model, [25], to model the flame wrinkling factor, Ξ, at both scales δ_u^0 and δ_u^F. It however appears as if the intrinsic details of the model used for Ξ is of less importance to the overall behavior of the TFM model as it is used to evaluate the flame wrinkling at neighboring scales.

The Partially Stirred Reactor (PaSR) model is derived from a cartoon of turbulent mixing and combustion provided by experimental, [26-27], and DNS data, [28-29]; Hence, turbulent reacting flows may be viewed as a muddle of vortex structures of different character (sheets, ribbons and tubes) in which the tubes and ribbons carry most of the high-intensity vorticity and dissipation. Regions of high exothermicity and volumetric expansion are found in small structures distributed among the fine-structure vortices whereas regions of low exothermicity can be distributed more randomly, [29]. Hence, the reacting flow is divided into fine-structures (*), responsible for mixing and chemical reactions, provided a sufficiently high temperature, embedded into a surrounding fluid (^{0}). Thus,

$$\overline{\dot{w}_j(\rho,T,Y_i)}=\int_\rho\int_T\int_{Y_i}\wp(\rho,T,Y_i)\dot{w}_j(\rho,T,Y_i)d\rho dT dY_i=\gamma^*\dot{w}_j(\overline{\rho},T^*,Y_i^*)+(1-\gamma^*)\dot{w}_j(\overline{\rho},T^0,Y_i^0), \quad (4)$$

in which γ^* is the reacting subgrid volume fraction. The conditions in the fine structures and surroundings are connected by the subgrid equations, $\overline{\rho}(Y_i^*-Y_i^0)/\tau^*=\dot{w}_i(\overline{\rho},Y_i^*,T^*)$ and $\overline{\rho}\Sigma_{i=1}^N(Y_i^*h_i^*-Y_i^0h_i^0)/\tau^*=\Sigma_{i=1}^N h_{i,f}^\theta\dot{w}_i(\overline{\rho},Y_i^*,T^*)$ in which τ^* is the subgrid time. By defining the resolved fields as $\tilde{\phi}=\gamma^*\phi^*+(1-\gamma^*)\phi^0$, the subgrid balance equations becomes,

$$\begin{cases}\overline{\rho}(Y_i^*-\tilde{Y}_i)=(1-\gamma^*)\tau^*\dot{w}_i(\overline{\rho},Y_i^*,T^*),\\ \overline{\rho}\Sigma_{i=1}^N(Y_i^*h_i^*(T^*)-\tilde{Y}_i\tilde{h}_i(\tilde{T}))=(1-\gamma^*)\tau^*\Sigma_{i=1}^N h_{i,f}^\theta\dot{w}_i(\overline{\rho},Y_i^*,T^*).\end{cases} \quad (5)$$

To close the PaSR model (5), the subgrid time, τ^*, and the reacting volume fraction, γ^*,

needs to be provided. The subgrid time scale is assumed to be the geometrical mean of the time-scale of the shear, $\tau_\Delta = \Delta/v'$, and that of the Kolmogorov scale, $\tau_K = (\nu/\varepsilon)^{1/2}$, to cover the whole span of time scales, so that $\tau^* \approx \sqrt{\tau_K \tau_\Delta} \approx \nu^{1/4}\Delta^{3/4}v'^{-5/4}$. The reacting volume fraction is here defined as $\gamma^* \approx \Delta V^*/\Delta V$, where ΔV^* is the volume of fine structures in the volume ΔV. If we estimate the fine structure volume as $\Delta V^* \approx \tau_c \dot{m}/\overline{\rho}$ and the total volume as $\Delta V \approx (\tau^* + \tau_c)\dot{m}/\overline{\rho}$, in which $\dot{m} \approx \overline{\rho}\Delta S^* |\tilde{\mathbf{v}}|$ is the mass-flow through the fine-structure surface ΔS^* and $\tau_c \approx \nu/s_u^2$ is the approximate chemical time scale, then $\gamma^* \approx \tau_c/(\tau^* + \tau_c)$. Inserting the expressions for τ^* and τ_c results in that $\gamma^* \approx \beta(\ell_K/\Delta)$ with β a coefficient. The filtered species transport equations can then finally be expressed as,

$$\partial_t(\overline{\rho}\tilde{Y}_i) + \nabla\cdot(\overline{\rho}\tilde{\mathbf{v}}\tilde{Y}_i) = \nabla\cdot(D_i\nabla\tilde{Y}_i - \mathbf{b}_i) + M_i P_{ij}[\gamma^* \dot{w}_j(\overline{\rho}, Y_i^*, T^*) + (1-\gamma^*)\dot{w}_j(\overline{\rho}, Y_i^0, T^0)]. \quad (6)$$

Comparing $\dot{w}_j(\overline{\rho}, Y_i^*, T^*)$ and $\dot{w}_j(\overline{\rho}, Y_i^0, T^0)$ we find that the first term dominates (due to the exponential dependence of $\dot{w}$ on T) so that the second term can safely be neglected.

3. COMBUSTION CHEMISTRY

Accurate predictions of combustor temperatures, emissions, self-ignition as well as flame-holding phenomena require the use of carefully selected reaction mechanisms. Single step mechanisms are not sufficiently accurate to capture these and similar features whereas detailed mechanisms are too complicated and expensive to handle. For example, hydrogen-air combustion involves 8 species and 38 reactions, [30], whereas for methane-air, 53 species and 325 reactions are suggested, [31]. For a realistic jet fuel (which is a blend of many hydrocarbons) the number of species and the reaction mechanism itself is growing, and recently Lu & Law, [32], proposed a mechanism with 561 species and 2539 reactions. Reduced mechanisms consisting of a limited number of species and reaction steps are thus needed, and can be achieved in different ways. Systematic mechanism reduction originates in the detailed mechanism that is simplified by means of either Intrinsic Low Dimensional Manifold (ILDM) methods, [33], reduction through quasi-steady state and quasi-equilibrium analysis, [34], reduction by sensitivity analysis, [35], or computational singular perturbation methods, [36]. Although accurate, these methods often result in complicated reaction rate models involving equilibrium expressions thus being rather complicated to implement in an LES code. Another approach is to use a global mechanism, including the species of interest, and to fit the Ahrrenius rate parameters so that the behavior of the detailed mechanism is mimicked over a range of equivalence ratios. Meredith & Black, [37], has proposed such an algorithm with the Ahrrenius rate parameters computed from an optimization algorithm coupled to a detailed kinetic calculation. Here, we will use such optimized global reaction mechanism and a single step NO formation mechanism (when appropriate), [38], to estimate the amount of NO formed during combustion.

4. NUMERICAL METHODS

For this study we use the C++ library OpenFoam, [39], as the computational platform, that

has previously been used for applications of varying complexity, e.g. [8, 40-41]. The code uses an unstructured collocated Finite Volume (FV) method, [37], in which the discretization is based on Gauss theorem. Given the vector of unknowns, $\overline{\mathbf{u}}=[\overline{\rho}, \overline{\rho}\tilde{Y}_i, \overline{\rho}\tilde{\mathbf{v}}, \overline{\rho}\tilde{E}]^T$, the semi-discretized equations can be compactly expressed as,

$$\partial_t(\overline{\mathbf{u}}_P)+\tfrac{1}{\delta V_P}\Sigma_f[\mathbf{F}_f^C(\overline{\mathbf{u}})-\mathbf{F}_f^D(\overline{\mathbf{u}})+\mathbf{F}_f^B(\mathbf{u},\overline{\mathbf{u}})]=s_P(\mathbf{u},\overline{\mathbf{u}}), \quad (7)$$

where $\mathbf{F}_f^C(\overline{\mathbf{u}})$, $\mathbf{F}_f^D(\overline{\mathbf{u}})$, $\mathbf{F}_f^B(\mathbf{u},\overline{\mathbf{u}})$ and $s_P(\mathbf{u},\overline{\mathbf{u}})$ are the convective, diffusive, subgrid fluxes and source terms, respectively. For low Mach number flows a semi-implicit code based on a second order accurate Crank-Nicholson time-integration scheme and a PISO procedure utilizing a Rhie & Chow interpolation for the cell-centered data storage structure, [42], is used, and for high Mach-number flows a fully explicit code based on a second order accurate TVD Runge-Kutta scheme, [43], is used. In both cases, the convective fluxes are reconstructed by a monotonicity preserving scheme $\mathbf{F}_f^C(\overline{\mathbf{u}})=\mathbf{F}_f^{C,H}(\overline{\mathbf{u}})-(1-\Psi)[\mathbf{F}_f^{C,H}(\overline{\mathbf{u}})-\mathbf{F}_f^{C,L}(\overline{\mathbf{u}})]$, [44], with $\mathbf{F}_f^{C,H}(\overline{\mathbf{u}})$ being a 2nd order linear reconstruction, $\mathbf{F}_f^{C,L}(\overline{\mathbf{u}})$ a 1st order upwind biased reconstruction and Ψ a non-linear flux limiter. The flux limiter is used to switch between the flux reconstruction schemes, and here the MC limiter, [45], is used for the momentum, energy and species equations whereas only the higher order scheme is used for the continuity equation. To minimize the non-orthogonality errors in the viscous and subgrid fluxes, $\mathbf{F}_f^D(\overline{\mathbf{u}})$ and $\mathbf{F}_f^B(\mathbf{u},\overline{\mathbf{u}})$ are split into orthogonal and non-orthogonal parts, [44]. Central difference approximation and gradient face interpolation are used for the orthogonal and non-orthogonal parts, and both codes use collocated cell-centered variable arrangement and a fixed time step often corresponding to a Courant number of ~0.3.

5. VERIFICATION AND VALIDATION

The computational methodology used, involving the OpenFoam platform, [39], has been verified for a range of cases using systematic grid refinement studies, the method of manufactured solutions and modified equations analysis to estimate the truncation errors. The application codes are extensively validated against DNS and experimental data and many such cases have been reported earlier such as, [46-55].

Figure 1 shows selected results from LES of an axisymmetric dump combustor experimentally studied by Gould *et al*, [56-57], for a premixed CH_4-air mixture at Re=55,800. The chemistry consists of a two-step mechanism, $CH_4+1.5O_2 \rightarrow CO+2H_2O$ and $CO+0.5O_2 \leftrightarrow CO_2$, with parameters and St numbers determined from the Gri 3.0 mechanism. According to figure 1a an annular recirculation region forms at the dump-plane, bounded by the wall and the annular shear-layer that evolves from the roll-up of the contraction wall vorticity. This shear-layer is accountable for the mixing between cold reactants and hot products, and due to the high strain-rates in the shear-layer ignition is delayed, allowing Kelvin-Helmholtz (KH) instabilities to develop. The vorticity is dominated by annular vortex-rings, developing from the KH instabilities, whereas inbetween vortex rings secondary vortices develop that disfigures the next ring. Vortex-stretching and baroclinic torque effects further modify the vorticity so that further downstream the vorticity consist of a collection

of staggered Ω-shaped structures with their legs parallel to the combustor wall and its neck inclined towards the flame. Exothermicity occurs some distance downstream, within the vortex structures, and the flame anchors at the dump-plane due to the recirculation of hot combustion products. In figure 1b and 1c comparisons between predicted and measured first and second order statistical moments of velocity and temperature are presented. Good agreement is obtained for both finite rate chemistry models whereas the reference flamelet LES, show less accurate agreement with the experimental data. The combustion dynamics is a combination of system acoustics, dominated by the longitudinal mode frequency of 66 Hz, and flow instabilities, dominated by the KH instabilities, having a roll-up frequency of ~165 Hz, close to 180 Hz as suggested by linear stability theory, [58].

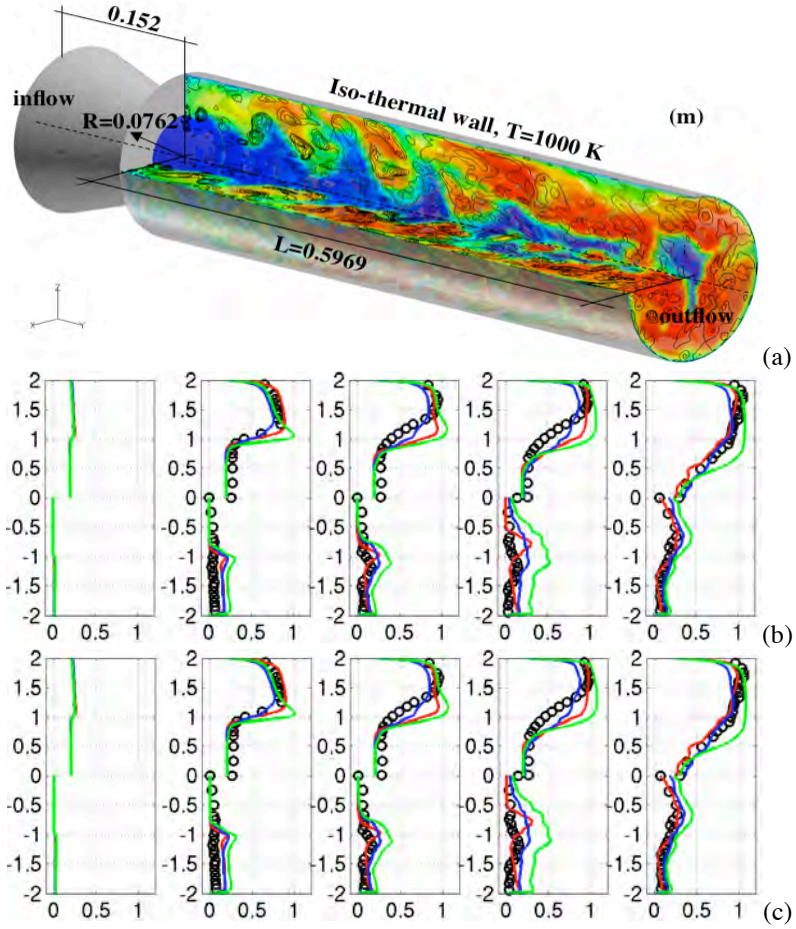

Figure 1. (a) Perspective view of the axisymmetric dump-combustor, cut-open to illustrate the reacting flow in terms the instantaneous temperature and vorticity. (b) Normalized mean axial velocity profiles (upper half) and axial rms-fluctuation profiles (lower half) and (c) normalized (by the adiabatic flame temperature) mean temperature profiles (upper half) and temperature rms-fluctuation profiles (lower half) at x/R/2=0.0, 1.0, 3.0, 5.0 and 12.0. Legend: experimental data, [32], (○), PaSR-LES (—), TFM-LES (—) and flamelet-LES (—).

Figure 2 shows some results from LES of a low-swirl burner, [59-60], which consists of an outer annular swirler with eight swirl-vanes and an inner perforated plate that allows for 40% by volume of the premixed CH_4-air mixture to pass, resulting in a swirl number of

0.5. Several experimental, [59-60], studies have been performed for this burner making it a good validation case, [54, 61]. The PaSR- and TFM-LES are based on the two-step mechanism $CH_4+1.5O_2 \rightarrow CO+2H_2O$ and $CO+0.5O_2 \leftrightarrow CO_2$, with rate parameters resulting in the same laminar flame speed as used in the flamelet LES. All LES (a representative image from the PaSR LES is shown in figure 2a) and experiments indicate a fully detached flame, with the peak temperature at the rich leading edge of the flame. The flame is bowl shaped as a result of the velocity distribution. Strong 3D wrinkling of the flame front is observed in both the LES and in the data, [60]. Downstream of the high temperature zone, a weak recirculation zone, in which the reactants mix with the ambient air, is observed in all LES. This results in a leaner mixture with lower temperature in the downstream part. The flame oscillates around its mean location defined by its lift-off height ~0.64D and appears not to be dependent on the recirculation region to stabilize. Instead, the flame stabilize by the inner shear layer, originating at the swirler exit, that rolls-up into large scale vortical structures that interacts with the flame. Further out in the swirling jet, the flame is pushed down, whereby some fuel mixes with ambient air prior to the reaction zone, and is diluted beyond

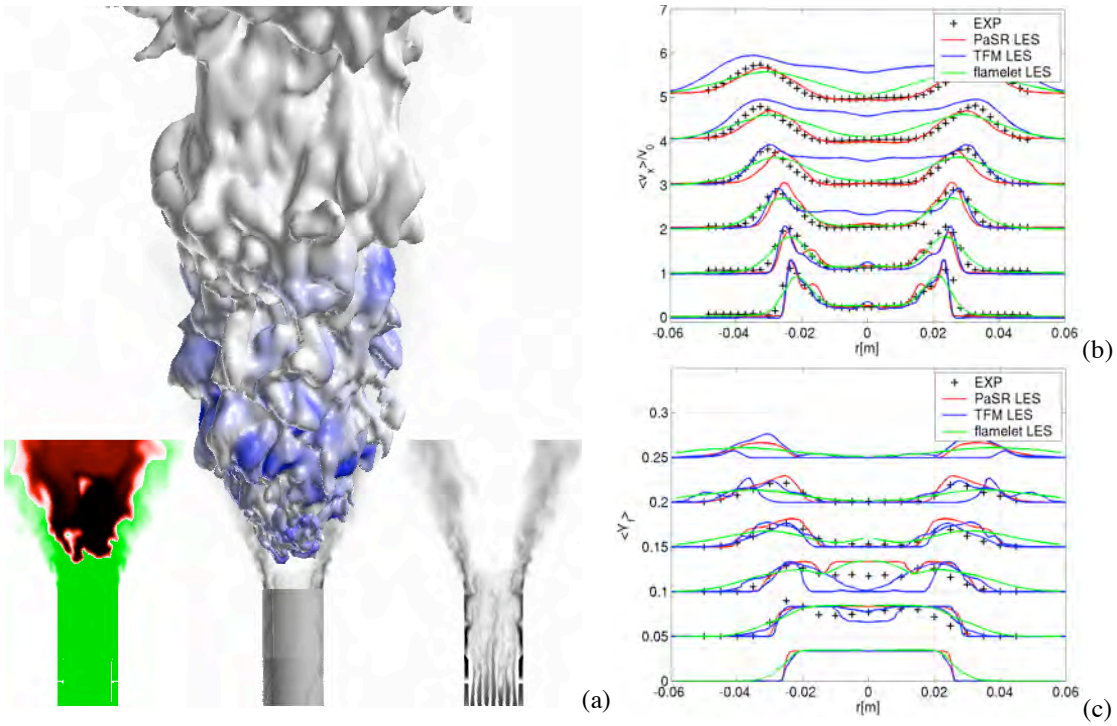

Figure 2. (a) Side view of the low-swirl burner in terms of an iso-surface of the temperature colored by the NO concentration together with distributions of OH and fuel concentrations (left) and the axial velocity (right). (b) Time averaged axial velocity and (c) fuel concentration at six cross-sections (x/D=0.2, 0.4, 0.6, 0.8, 1.0 and 1.2) downstream of the burner rim.

the flammability limit, as confirmed by the acetone fuel tracer LIF, [61]. Figures 2b and 2c compares the time-averaged axial velocity and fuel concentration, respectively, revealing that the PaSR-LES agrees very well with the experimental data whereas the TFM-LES and the flamelet LES disagree with the data at some distance downstream of the burner rim.

The reason for this disagreement is that these models do not capture the turbulent flame speed, the prediction of which is crucial for predicting the lift-off height.

6. MULTI-BURNER ANNULAR GAS TURBINE COMBUSTOR APPLICATION

Annular gas turbine combustors are used for aero- and marine propulsion, and power generation, and to reduce emissions most gas turbines operate close to the lean stability limit, making them vulnerable to combustion instabilities that may lead to blowout, flashback and vibrations. Combustion oscillations have been studied theoretically, experimentally and computationally for can combustors and single burner configurations, [62], and are quite well understood. However, only little is known about their behavior in multi-burner annular combustor configurations, representative of real engines. Based on the tests described in [63] and the work done by Staffelbach *et al*, [64], it seems that the LES approach is mature enough to approach the problem of fully annular multi-burner configurations. As part of the European Commission 6th framework programme Cost Effective Small AiRcraft (CESAR), [65], we have investigated a fully annular multi-burner turbo-shaft engine combustor. The Jet A-air combustion chemistry is modeled by a three step mechanism: $C_{12}H_{23}+11.75O_2 \rightarrow 12CO+11.5H_2O$, $CO+0.5O_2 \rightarrow CO_2$ and $O_2+N_2 \rightarrow 2NO$, [66], taking into consideration the primary emissions of CO, CO_2 and NO.

Figure 3a presents an overview of the reacting flow in the fully annular configuration with 12 interacting flames, and a comparison between the flame in sector 12 of the annular configuration (upper insert) with the corresponding flame from a single sector LES (lower insert). Although similar, the flame in the fully annular configuration is different due to the (azimuthal) pressure oscillations in the annular combustor. According to figure 3b the flow is dominated by vorticity initiated from the fuel nozzle, where the inner, strongly swirling, jet, discharging through the core of the fuel nozzle, provides fuel to the base of the flame, and vortex breakdown just downstream of the fuel nozzle. The vortex breakdown results in the formation of weakly interacting central recirculation zones dominating the flow between the fuel nozzle and the first row of dilution holes. The outer air jet, discharging through the fuel nozzle, serves the purpose of creating a large toroidal-shaped vortex structure that form between the jet, dump plane and fuel nozzle, which together with the central recirculation zone is responsible for stabilizing the diffusion flame.

The combustion dynamics reveal that in the first stage of the flame tube (between the dump plane and the first row of dilution holes) the fuel was consumed at the flame front, resulting in heat-release, volumetric expansion, baroclinic torque effects, flame generated turbulence, increased viscosity, mass diffusion and thermal diffusivity, as well as the formation of hot combustion products. This stratified fuel distribution surrounds the flame and aids in reducing CO_2 and NO. In the second stage of the flame tube (i.e. between the first row of dilution holes and the turn of the flame tube), the hot reaction products were cooled and diluted by air supplied through the dilution and film cooling holes, providing a thermal boundary layer between the flame-tube wall and the hot combustion products protecting the flame-tube wall. In the third stage of the flame-tube (i.e. turn of the flame tube

and the flame tube outlet or turbine inlet) the hot combustion products accelerated due to the volumetric expansion towards the outlet.

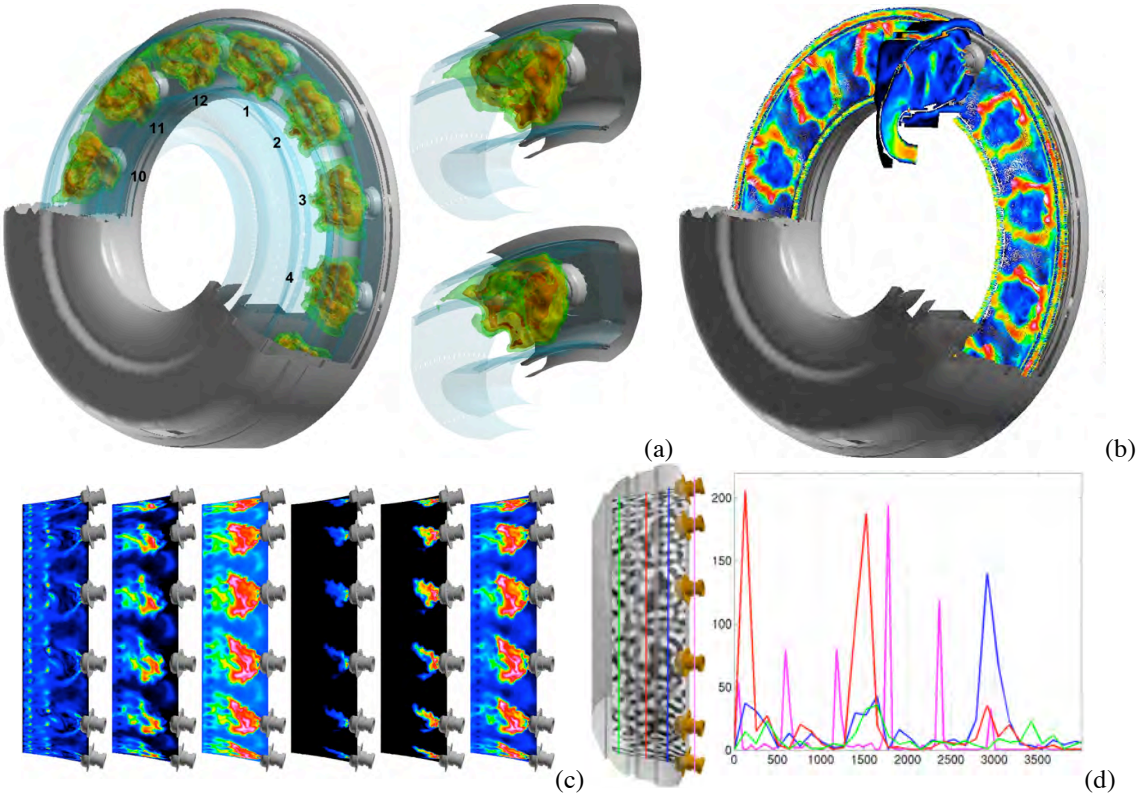

Figure 3. Single and fully annular combustion simulations of CESAR combustion chamber. (a) Instantaneous semi-transparent iso-surfaces of the temperature at 2500 K, 2000 K, 1500 K and 1000 K for (center) multi-burner annular combustor (upper) enlargement of burner 12, and (lower) results from single sector combustor simulation. (b) Instantaneous velocity vector plots colored by the velocity magnitude at two planes for (center) multi-burner annular combustor (upper) enlargement of burner 12, and (lower) results from single sector combustor simulation. (c) Contours of the (from left to right) velocity magnitude, NO mass fraction, temperature, fuel mass fraction, CO mass fraction, and CO_2 mass fraction on a conically shaped plane parallel to centerlines of the air-fuel nozzles. (d) Semi-transparent side view illustrating the pressure fluctuations inside the annular combustor and spectral composition of the pressure field in the combustor. Legend: (—) close to the fuel nozzle, (—) mid combustor, (—) rear combustor and (—) between flame tube and combustor casing.

The fully annular multi-burner results exhibited a more complicated flow field due mainly to burner-to-burner interactions and azimuthal pressure oscillations. The flame dynamics was found to be dominated by the local equivalence ratio, the pressure fluctuations and the velocity gradients in the shear layers surrounding the flames. The significance of the pressure fluctuations is clear from figure 3d and azimuthal pressure fluctuations around 950 Hz are observed to cause the flames to pulsate in phase with each other, hence amplifying the unsteady dynamics. Other flow features that result from the neighboring burners include modified toroidal vortex structures around the flames and modified central recirculation regions. In figures 3a and 3b, a comparison between the single-sector and fully annular multi-burner LES predictions reveals that these results are fairly similar but with im-

portant differences. For example, the jets discharging from the dilution and mixing holes do not penetrate as deep in the fully annular multi-burner configuration as they did in the single sector configuration. Due to the azimuthal pressure fluctuations the pressure drop over the individual air-fuel nozzles may vary thereby redirecting the flow of air to different burners according to the pressure drop and the pressure fluctuations. This was found to be affecting the mixing and the local equivalence ratio that in turn modified the reaction rates and the exothermicity leading also to a different volumetric expansion.

7. HIGH-SPEED RAM- AND SCRAMJET COMBUSTION

High-speed flight has for along time been of interest to man - both for terrestrial travel and space exploration and transport. Key issues for these types of travel are the vehicle design and the propulsion system, and how to integrate the two. Two types of propulsion systems, ramjets, [67], and scramjets, [68], are suitable for such vehicles. In a ramjet the flow is decelerated to subsonic levels before it enters the combustor, allowing an operational regime of $3<Ma<5$, above which the deceleration leads to excessive thermal losses, whereas in a scramjet the flow through the engine remains supersonic, allowing an operational regime of $6<Ma<15$. Seamless integration of ram- and scramjet operation is potentially possible in the same engine, [69], by allowing it to change mode accordingly.

Figure 4 presents selected aspects of the reacting flow in the HyShot II combustor, [70], as obtained from recent combined RANS and LES computations, [71]. This configuration corresponds to the post-flight analysis performed in the HEG, [72], at an altitude of 32.5 km. Due to the complexity of simulating the reacting flow in the HyShot scramjet in the HEG facility a zonal approach was adopted in [71], in which RANS (using the non-equilibrium 5-species, 5-step reaction mechanism of Gupta *et al*, [73],) was performed in the HEG nozzle section and in the HEG test section to obtain the initial and boundary conditions for the HyShot II combustion LES. For these simulations, the reduced 7-species and 8-step H_2-air mechanism of Davidenko *et al*, [74], was employed as it has successfully been used in supersonic combustion LES before, [23].

The wall pressure in figure 4a shows that the pressure increases slowly with increasing distance from the transverse fuel jets to increase more rapidly between 30 and 60D downstream of the transverse fuel jets to peak at about 100D. Higher wall pressures are observed under the bow shock, forming a hood over the transverse fuel jet and beneath the fuel jets. The more rapid pressure increase further downstream is caused by rapid volumetric expansion due to exothermicity. The time-averaged transverse H_2 jets typically consist of a counter-rotating vortex pair and a horseshoe-vortex, whereas instantaneously they consist of smaller and topologically more complex vortex structures, cf. figure 4a. These in turn consist of small bent S-shaped vortices (side arms) with their lower parts aligned with the flow and their upper parts curling over the jet forming the neck (circumferential rollers) of the counter-rotating vortex pair. This feature is observed experimentally by Ben-Yakar *et al*, [75], and they propose that the side arms are stretched by increased shear stresses in the regions of steep velocity gradient. These vortical structures seem to arise from Kelvin-

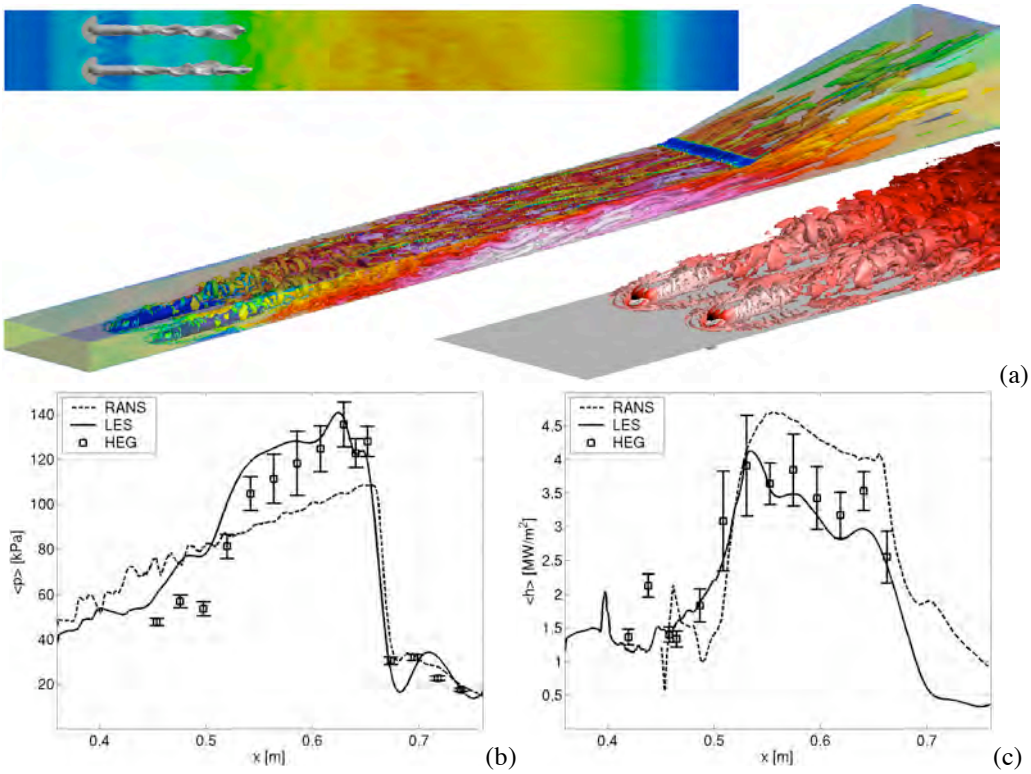

Figure 4. Scramjet propulsion. (a) Composite figure of the reacting flow in the HyShot II combustor in terms of wall pressure and an iso-surface of the H_2 mass fraction, iso-surface of the second invariant of the velocity gradient, λ_2, colored by the temperature and iso-surfaces of the H_2 mass fraction (gray) and the heat release conditioned on λ_2. (b) Comparison of predicted and measured wall pressures between jet injectors and (c) comparison of heat flux along a line 6.0 mm off centerline between jet injectors.

Helmholz (KH) instabilities in the jet shear layers just beneath the bow-shock. Since the transverse jets contain all the H_2, mixing dominates during the first 20 to 40D, whereby air is entrained into the vortex structures and H_2 diffuses into the air, resulting in a combustible mixture around the jets. Further downstream, between 30 and 60D, H_2 and air are sufficiently mixed to burn if the temperature is sufficiently high and the H_2 jets are observed to penetrate to 1/3 of the combustor height before self-ignition. In this region, self-ignition occurs intermittently with the assistance of hot recirculated products. Self-ignition seems to be triggered by hot-spots in regions of colliding shocks which ten explain the unsteady nature of the self-ignition region. The volumetric expansion causes the S-shaped side arms and spanwise rollers to merge into Ω-shaped vortices, dominating the self-ignition region. Due to volumetric expansion, vortex stretching, baroclinic torque and self-diffusion, the vortex structures eventually develop into longitudinal vortices, dominating the downstream part of the combustor. These vortices grow in size with increasing distance from the injection point due to the volumetric expansion, and when they reach the end of the combustor, the gradual expansion increases the velocity, presented in figure 4a, causing a forward directed thrust on the thrust surface forming the nozzle.

In figures 4c and 4d, predicted and measured axial profiles of the time-averaged wall

pressure and heat flux are compared at lines on the bottom wall of the combustor between injectors and 6.0 mm off centerline, respectively. For the time-averaged wall pressure the experimental data show a sudden increase between x=0.50 and 0.53 followed by a slower increase up to the end of the combustor, at x=0.65, after which the pressure drops rapidly to the exhaust pressure. The RANS predictions show an almost linear increase from the combustor inlet to the combustor exit, missing the sharp pressure increase indicating combustion, and under- or overpredicting the wall pressure by up to 25%. For the time-averaged wall heat flux a sudden rise is found at x≈0.52, corresponding well to the location at which the pressure rises due to combustion. The average level in the first part of the combustor agrees well with the laminar heat flux predicted using a Blasius profile and a wall temperature of 300 K, but the transverse H_2 jet introduces some peculiarities after x=0.42. The RANS predictions typically overpredict the heat flux whereas the LES typically underpredict the heat flux, with between 15% and 10%, respectively. Both the pressure and heat flux predictions are within the experimental uncertainty.

8. AFTERBURNING BEHIND CONDENSED PHASE EXPLOSIONS

Our knowledge of condensed phase explosions is limited although explosives have existed since the gunpowder was discovered in China in the 9th century. During the early stages of an explosion the solid or liquid explosive material is rapidly transformed to a hot, dense, high-pressure gas, rich in solid carbon, carbon monoxide and hydrocarbons. The explosion products expand at high velocities aiming at pressure equilibrium with the surrounding air, causing a radially expanding supersonic shock-wave, [76]. Only a limited part of the stored chemical energy is released in the detonation. The residual energy is released more slowly as the detonation products mix with the ambient air and subsequently burn, [77]. This afterburning process has little effect on the initial blast as it occurs slower than the primary detonation. Later stages of the blast can be affected by afterburning, particularly for confined space explosions, [78], and in the proximity of the ground. As the blast expands, the pressure drops rapidly due to geometric divergence, work done by compressing the air and dissipation of energy in heating the air.

Simulations of afterburning behind an explosive air blast in free air and near the ground of TNT and HMX were conducted in [79], and here selected results from the TNT simulations are presented. A 0.12 m diameter spherical charge was detonated in air and left to burn through the two-step reaction $C+0.5O_2 \rightarrow CO$ and $CO+0.5O_2 \rightarrow CO_2$. For the free air blast, figure 5a reveals that the outgoing blast wave (white rings in ∇p) heats up and accelerates the ambient air as it propagates through it. Early in the process (at 0.4 ms) a rarefaction wave (dark blue region in ∇p) propagates inwards, boosting the acceleration caused by the blast wave and later forcing an outward directed acceleration of the hot gases. From the CO_2 distribution at times 0.4 and 0.8 ms, the interface between the detonation products and the shock-compressed air is impulsively accelerated, resulting in Rayleigh-Taylor (RT) instabilities, [80], due to the impulsive acceleration of the contact surface. The results suggest that a short time after the initial blast the ingoing rarefaction wave overexpands caus-

ing a secondary shock (light blue), resulting in the formation of a thin mixing layer, initially seen at 0.4 ms in the CO_2 distribution, between the initial blast wave and the second-

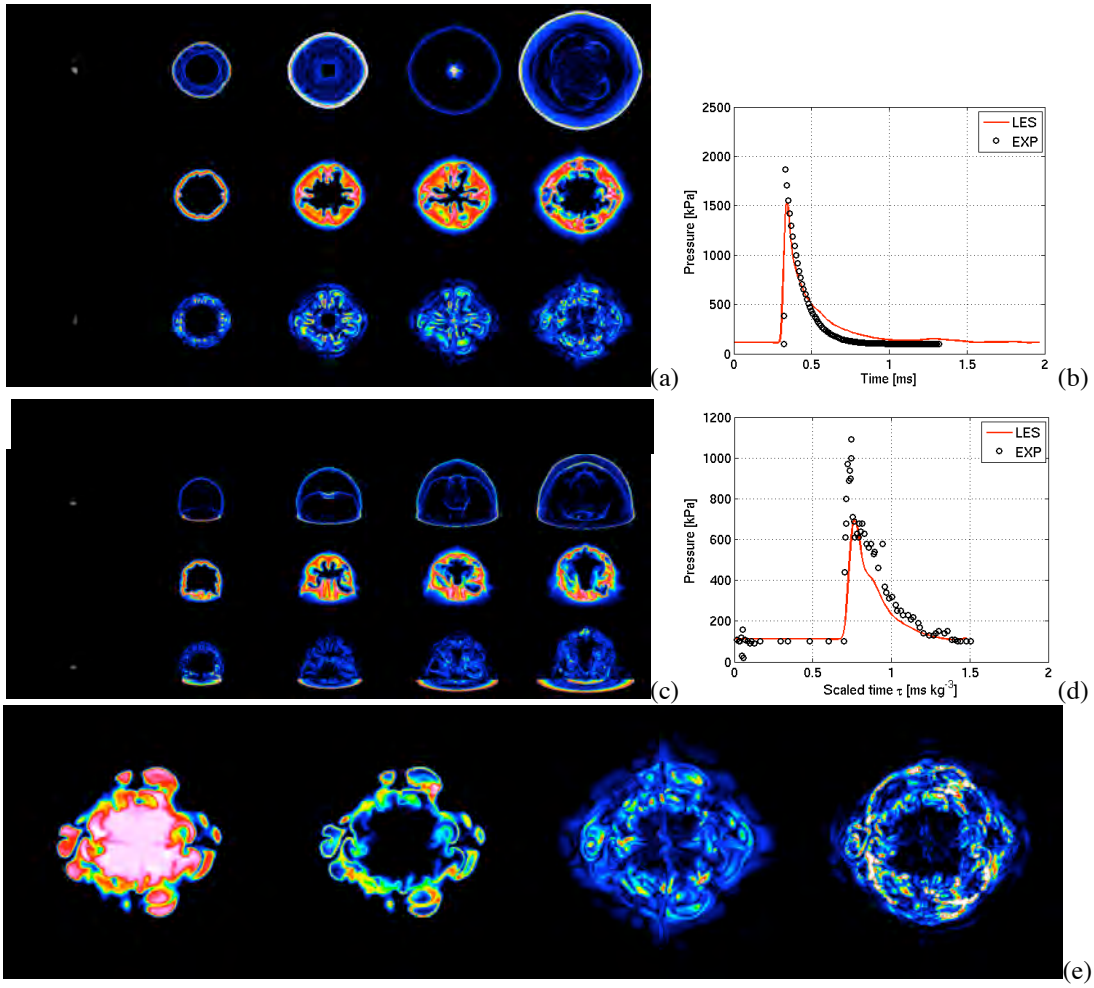

Figure 5. Afterburning in condensed phase air blast of TNT. (a) Free air blast featuring from top down: pressure gradient, mass fraction of CO_2 and vorticity at different times, times from left to right are 0.0 ms, 0.4 ms, 0.8 ms, 1.2 ms and 2.0 ms. (b) Validation against experimental data [83] of pressure at radius of 0.9 m. (c) Near ground blast featuring from top down: pressure gradient, mass fraction of carbon dioxide and vorticity at different times, times from left to right are 0.0 ms, 0.5 ms, 1.0 ms, 1.5 ms and 2.0 ms. (d) Validation against experimental data [84] of scaled [85] pressure and time. (e) Analysis of mixing and afterburning featuring from left to right: mass fraction of carbon, heat release, magnitude of vorticity and baroclinic term.

-ary shock. The secondary shock will eventually strengthen by means of detonation product gases accelerating it, and the shock will further strengthen to the point of implosion (at ~1.2 ms). The implosion further entrains air into the mixing layer (between 0.8 ms to 1.2 ms in the vorticity distribution), enhancing the afterburning (at 0.8 and 1.2 ms). When the secondary shock reflects from the origin (at 1.2 ms) this is redirected outwards (at 2.0 ms) to interact with the existing RT instabilities, depositing vorticity into the mixing layer due to a misaligned pressure (baroclinic torque effects), giving rise to Richmeyer-Meshkov

(RM) instabilities, [81]. At later stages (>2.0 ms) the remaining fuel is consumed in the core of the explosion in an almost constant-pressure mixing layer.

Figure 5c illustrates the results of the semi-confined TNT explosion. The initial blast wave expands outwards in the air as well as parallel to the ground. After the blast wave is reflected by the ground (at 0.5 ms) it propagates inwards, initially as two separate shock waves, into the mixing layer, creating behind it a low pressure region that entrains air into the combustion zone. This effect is seen as a mushroom shaped fireball, visible e.g. in the CO_2 distribution at 1.0 ms. The ground reflected shock collide (at 1.0 ms) forming a complex mixing zone around the collision point (seen in the vorticity and ∇p), and two new shocks are formed, one propagating upwards and one downwards towards the ground. These shock systems form strong up- and downwashes of the detonation products that enhances the mixing (development seen from 1.0 ms to 2.0 ms in pressure gradient and vorticity distributions). Even here the RT instabilities are created between in the burning interface and the propagation of the ground reflected shock upwards gives rise to the misaligned pressure and density gradients, creating RM instabilities, [82]. Following ∇p, the vorticity expands parallel to the ground, with an intense vorticity region found behind the surface blast wave and at the latest time also around the surface reshock region.

These simulation results have been validated against experiments with good agreement, as seen in figures 5b and 5d. The analysis of the mixing and afterburning, [79], concluded that RT instabilities generated during explosion event gave rise to vorticity and mixing, where the vorticity was found to be formed by exothermicity due to misaligned pressure and density gradients. The analysis also indicates that the heat release and the combustion take place around the vorticity filaments, demonstrated in figure 5e, predicting afterburning and mixing behind a blast wave. The near surface explosions showed that the patterns and features involved in mixing and combustion are similar as for the free air explosion. The proximity to the ground affects the pressure distribution, [85], and a different shock propagation pattern, which gives the combustion region a mushroom shape, however the heat release is still oriented around the vorticity structures.

9. CONCLUDING REMARKS

Here we present LES predictions of both multi-burner annular gas turbine combustor, high-speed combustion in a simplified scramjet engine and afterburning behind condensed phase explosions. The combustion LES models employed are based on finite rate chemistry models, making use of the partially stirred reactor and thickened flame models, and implemented in OpenFOAM. Good agreement with the (limited) reference data available for the three combustion configurations is found. In order to further validate the combustion LES models, comparisons are made with experimental data in various laboratory combustors, such as a premixed axisymmetric dump combustor and an open low-swirl burner, resulting in a stratified mixture. The good agreement obtained in the validation studies gives confidence to the LES methodology and the ability to predict combustion under realistic, yet somewhat simplified, conditions. The predictions obtained for the multi-burner annular

combustor and scramjet engine are utilized to further elucidate the complex flow fields in these devices, which in turn may be used to direct the design of new combustor de-vices, to identify critical issues and to further improve the general understanding of the processes involved in combustion. Predictions of the afterburning behind the blast wave originating in a condensed phase explosion is used to improve safety and protect infrastructure through the use of improved predictions of structural loads and impulses.

ACKNOWLEDGEMENTS

The authors wish to acknowledge the Swedish Armed Forces and the Swedish Defense Material Agency for funding the research on condensed phase explosions and scramjets. S. Karl at DLR is acknowledged for successful collaboration on the HyShot II scramjet engine. The participants in the CESAR project, in particular S.A. Borzov, V.N. Gusev, T.V. Stepanova at Ivchenko-Progress, are acknowledged for their fruitful collaboration.

REFERENCES

[1] Hsu A.T., Anand M.S. & Razdan M.K.; 1997, "Calculation of a Premixed Swirl Combustor using the PDF Method, 42nd ASME Gas Turbines and Aeroengines Congress, June 2-5. Orlando, FL.

[2] Oevermann M.; 2000, "Numerical Investigation of Hydrogen Combustion in a SCRAMJET using Flamelet Modeling", Aerosp. Sci. Tech. **4**, p 463.

[3] Orth L. & Krier H.; 1998, "Shock Physics for Non-Ideal Detonations of Metalized Energetic Explosives", 27th Int. Symp. on Comb., p 2327.

[4] Sagaut P.; 2001, "Large Eddy Simulation for Incompressible Flows", Springer Verlag, Heidelberg.

[5] Grinstein F.F., Margolin L. & Rider B. (Eds.); 2007, "In Implicit Large Eddy Simulation: Computing Turbulent Fluid Dynamics", Cambridge University Press.

[6] Wilcox, D.C.; 1993, "Turbulence Modeling for CFD", DCW Industries.

[7] Oran E.S. & Boris J.P.; 1987, "Numerical Simulation of Reactive Flow", Elsevier, New York.

[8] Fureby C.; 2009, "LES Modeling of Combustion for Propulsion Applications". Phil. Trans. R. Soc. A, **367**, p 2957.

[9] Grinstein F.F. & Kailasanath K.K; 1994, "Three Dimensional Numerical Simulations of Unsteady Reactive Square Jets", Comb. & Flame, **100**, p 2.

[10] Garcia-Villalba M., Li N., Rodi W., Leschziner M.A.; 2009, "Large Eddy Simulation of Separated Flow over a Three-Dimensional Axisymmetric Hill", J. Fluid Mech., **627**, p 55.

[11] Alin N., Bensow R. Fureby C., Huuva T. & Svennberg U.; 2007, "Current Capabilities of RANS, DES and LES for Submarine Flow Simulations", J. Ship. Hydro., In Press.

[12] Bardina J., Ferziger J.H. & Reynolds W.C.; 1980, "Improved Subgrid Scale Models for Large Eddy Simulations", AIAA Paper No. 80-1357.

[13] Bensow R. & Fureby C.; 2007, "On the Justification and Extension of Mixed Models in LES", J. Turb **8**, N54.

[14] Schumann U.; 1975, "Subgrid Scale Model for Finite Difference Simulation of Turbulent Flows in Plane Channels and Annuli", J. Comp. Phys., **18**, p 376.

[15] Fureby C.; 2007, "On LES and DES of Wall Bounded Flows", Ercoftac Bulletin, March issue.

[16] Weller H.G., Tabor G., Gosman A.D. & Fureby C.; 1998, "Application of a Flame-Wrinkling LES Combustion Model to a Turbulent Shear Layer Formed at a Rearward Facing Step", 27th Int. Symp. on Comb, p 899.

[17] Hawkes E.R. & Cant R.S.; 2000, "A Flame Surface Density Approach to Large Eddy Simulation of Premixed Turbulent Combustion", Proc. Comb.. Inst. **28**, p 51.

[18] Knikker R. & Veynante D.; 2000, "Experimental Study of the Filtered Progress Variable Approach for LES of Premixed Combustion", in Advances in LES of Complex Flows, (Eds.) Friedrich R. & Rodi W., p 353.

[19] Wang P. & Bai X.S.; 2005, "Large Eddy Simulation of Turbulent Premixed Flames using Level-set G Equation", Proc. Comb. Inst. **30**, p 583.

[20] Colin O., Ducros F., Veynante D. & Poinsot T.; 2000, "A Thickened Flame Model for Large Eddy Simualtions of Turbulent Premixed Combustion", Phys. Fluids **12**, p 1843.

[21] Sankaran V. & Menon S.; 2005, "Subgrid Combustion Modeling of 3D Premixed Flames in the Thin-Reaction-Zone Regime", Proc. of the 30th Int Symp on Comb, p 575.

[22] Givi P.; 2006, "Filtered Density Function of Subgrid Scale Modeling of Turbulent Combustion", AIAA.J., **44**, p 16.

[23] Berglund M., Fedina E., Fureby C., Sabel'nikov V. & Tegnér J.; 2010, "Finite Rate Chemistry Large-Eddy Simulation of Self-Ignition in Supersonic Combustion Ramjet", AIAA.J., **48**, p 540.

[24] O'Rourke P.J. & Bracco F.V.; 1979, "Two Scaling Transformations for the Numerical Computation of Multidimensional Unsteady Laminar Flames", J. Comp. Phys., **33**, p 185.

[25] Fureby C.; 2004, "A Fractal Flame Wrinkling Large Eddy Simulation Model for Premixed Turbulent Combustion", Proc. of the 30th Int Symp on Comb, p 593.

[26] Batchelor G.K. & Townsend A.A.; 1947, "Decay of Vorticity in Isotropic Turbulence", Proc. Roy. Soc. London Ser A, **190**, p 534.

[27] Kuo Y.S. & Corrsin S.; 1971, "Experiments on Internal Intermittency and Fine Structures Distribution Functions in Fully Turbulent Fluid", J. Fluid Mech., **50**, p 285.

[28] Woodward P.R., Porter D.H., Sytine I., Anderson S.E., Mirin A.A., Curtis B.C., Cohen R.H., Dannevik W.P., Dimits A.M., Eliason D.E., Winkler K.-H., & Hodson S.W.; 2001 , "Very High Resolution Simulations of Compressible Turbulent Flows", Computational Fluid Dynamics, Proceedings of the 4th UNAM Supercomputing Conference Mexico City, June 2000, (Eds) Ramos E., Cisneros G., Fernandez-Flores A., & Santillan-Gonzalez A., p. 3 World Scientific.

[29] Tanahashi M., Fujimura M. & Miyauchi T.; 2000, "Coherent Fine Scale Eddies in Turbulent Premixed Flam-es", Proc. of the 28th Int Symp on Comb, p 5729.

[30] O Conaire M., Curran H.J., Simmie, J.M., Pitz W.J. & Westbrook C.K.; 2004, "A Comprehensive Modeling Study of Hydrogen Oxidation", Int. J. Chemical Kinetics, **36**, p 603.

[31] http://www.me.berkeley.edu/gri_mech/.

[32] Lu T. & Law C.-K.; 2008, "Strategies for Mechanism Reduction for Large Hydrocarbon: n-heptane". Comb. & Flame, **154**, p 153.

[33] Mass U. & Pope S.B.; 1992, "Implementation of Simplified Chemical Kinetics Based on Intrinsic Low Dimensional Manifold", 24th Int. Symp. on Comb., p 103.

[34] Chen J.-Y.; 1997, Workshop on Numerical Aspects of Reduction in Chemical Kinetics, CERMICS-ENPC Cite Descartes Champus sur Marne, France.

[35] Peters N.; 2000, "Turbulent Combustion", Cambridge University Press.

[36] Massias A., Diamantis D., Mastorakos E. & Goussis D.A.; 1999, "An Algorithm for the Construction of Global Reduced Mechanisms with CSP Data", Comb. Flame, 117, p 685.

[37] Meredith K.V. & Black D.L.; 2006, "Automated Global Mechanism Generation for use in CFD Simulations", AIAA 2006-1168.

[38] Miller J.A. & Bowman C.T.; 1989, "Mechanism and Modeling of Nitrogen Chemistry in Combustion," Progress in Energy and Combustion Science, **15**, p 287.

[39] Weller H.G., Tabor G., Jasak H. & Fureby C.; 1997, "A Tensorial Approach to CFD using Object Oriented Techniques", Comp. in Physics, **12**, p 629.

[40] Fureby C.; 2008, "Towards Large Eddy Simulation in Engineering", Prog. Aerospace Science, **44**, p 381.

[41] Fureby C. & Bensow R. 2008, "LES at Work: Quality Management in Practical LES", In Quality and Re-liability of Large Eddy Simulations, Eds. Meyers J., Geurts B & Sagaut P., p 239, Springer Verlag.

[42] Issa R.I.; 1986, "Solution of the Implicitly Discretised Fluid Flow Equations by Operator Splitting", J. Comp. Phys., **62**, p 40.

[43] Gottlieb S. & Shu C.-W.; 1998, "Total Variational Diminishing Runge-Kutta Schemes", Mathematics of Computation, **67**, p 73.

[44] Drikakis D., Fureby C., Grinstein F.F. & Liefendahl M.; 2007, "ILES with Limiting Algo¬rithms", In Implicit Large Eddy Simulation: Computing Turbulent Fluid Dynamics, Eds. Grinstein F.F., Margolin L. & Rider B., Cambridge University Press, p 94.

[45] Van Leer B.; 1977, "Towards the Ultimate Conservative Difference Scheme III. Upstream-Centered Finite-Difference Schemes for Ideal Compressible Flow", J. Comp. Phys., **23**, p 263.

[46] Drikakis D., Fureby C., Grinstein F.F. & Youngs D.; 2007 "Simulations of Transition and Turbulence Decay in the Taylor-Green Vortex with the MILES Approach", J. Turbulence **8**, p 1.

[47] Fureby C., Tabor G., Weller H. & Gosman D.; 1997, "A Comparative Study of Sub Grid Scale Models in Isotropic Homogeneous Turbulence", Phys. Fluids, **9**, p 1416.

[48] Fureby C., Alin N., Wikström N., Menon S., Persson L., & Svanstedt N.; 2004, "On Large Eddy Simulations of High Re-number Wall Bounded Flows", AIAA.J. **42**, p 457.

[49] Fureby C., Tabor G., Weller H.G. & Gosman D.; 1999, "Large Eddy Simulation of the Flow Around a Square Prism", AIAA.J, **38**, p 442.

[50] Persson T. M. Liefevendahl, Bensow R. & Fureby C., 2006, "Numerical Investigation of the Flow over an Axisymmetric Hill using LES, DES and RANS", J. Turbulence, **7**, p 1.

[51] Wikström N., Svennberg U., Alin N. & Fureby C.; 2004, "LES of the Flow past an Inclined Prolate Spheroid", J. Turbulence **5**, p 29.

[52] Fureby C., Knight D. & Kupiainen M.; 2007, "Compressible Turbulent Shear Flows", In Implicit Large Eddy Simulation: Computing Turbulent Fluid Dynamics, Eds. Grinstein F.F., Margolin L. & Rider B., Cambridge University Press, p 329.

[53] Fureby C., Henriksson M., Parmhed O., Sjökvist L. & Tegnér J.; 2008, "CFD Predictions of Jet Engine Exhaust Plumes", AIAA 2008-2345.

[54] Nogenmyr K-J., Fureby C., Bai., X.S., Petersson P. & Linné M.; 2009, "Large Eddy Simulation and Laser Diagnostic Studies on a Low Swirl Stratified Premixed Flame", Comb. Flame, **156**, p 25.

[55] Baudoin E., Nogenmyr K.J., Bai X.S. & Fureby C.; 2009, "Comparison of LES Models applied to a Bluff Body Stabilized Flame", AIAA 2009-1178.

[56] Gould R.D., Stevenson W.H., & Thompson H.D.; 1990, "Investigation of Turbulent Transport in an Axisymmetric Sudden Expansion", AlAA.J., **28**, p 276.

[57] Gould R.D., Stevenson W.H., & Thompson H.D.; 1983, "Laser Velocimeter Measurements in a Dump Combustor", 12th AIChE/ASME National Heat Transfer Conf., Paper 83-HT-47, Seattle, WA,

[58] Michalke A.; 1965 "On Spatially Growing Distributions in an Inviscid Shear Layer", J. Fluid Mech., **23**, p 521.

[59] Shepherd I.G., Cheng R.K., Plessing T., Kortschik C. & Peters N., 2002, "Premixed Flame Front Structure in Intense Turbulence",29th Int. Symp. on Comb., p 1833.

[60] Petersson P., Nauert A., Olofsson J., Brackman C., Seyfried H., Zetterberg J., Richter M., Dreizler A., Geyer D., Linne A., Aldén M. & Cheng R.K.; 2007, "Simultaneous PIV/OH-PLIF, Rayleigh Thermometry/OH-PLIF and Stereo PIV Measurements in a low-swirl flame", Applied Optics, **46**, p 3928.

[61] Nogenmyr, K., Peterson P., Bai X.S., Aldén M. & Fureby C.; 2008, "A Comparative Study of LES Turbulent Combustion Models Applied to a Low Swirl Lean Premixed Burner", AIAA-2008 0513.

[62] Candel, S.; 1992, "Combustion Instabilities Coupled by Pressure Waves and Their Active Control," 24th Int Symp on Comb., p 1277.

[63] Fureby C.; 2009, "LES of a Multi Burner Annular Gas Turbine Combustor", Flow Turb. & Comb., **84**, p 543.

[64] Staffelbach, G., Gicquel L.Y.M., Boudier G. & Poinsot T.; 2009, "Large Eddy Simulation of Self Excited Azimuthal Modes", 32nd Int Symp on Comb., p 2909.

[65] www.cesar-project.eu

[66] Cannon S.M., Smith C.E., Anand M.S.; 2003, "LES Predictions of Combustor Emissions in an Aero Gas Turbine Engine", AIAA 2003-4521.

[67] Fry R.S.; 2004, "A Century of Ramjet Propulsion Technology Evaluation", J. Prop. Power, **20**, p 27.

[68] Curran E.T.; 2001, "Scramjet Engines: The First Forty Years", J. Prop. Power, **17**, p 1138.

[69] Andreadis D.; 2007, "Scramjets Integrates Air and Space", The Industrial Physicist, **10**, p 24.

[70] Paull A., Alesi, H. & Anderson, S.; 2002, "The HyShot Flight Program and how it was Developed", AIAA-AAAF 11th Int. Space Planes and Hypersonic Systems and Technologies Conference, Orleans, France,

[71] Fureby C., Chapuis M., Fedina E. Karl S.; 2010, "CFD Analysis of the Hyshot II Combustor to the Proc. of the Comb. Inst. 33.

[72] Schramm J.M., Karl S., Hannemann K & Streelant J.; 2008, "Ground Testing of the HyShot II Scramjet Configuration in HEG", AIAA 2008-2547.

[73] Gupta R.N., Yos J.M., Thompson R.A. & Lee, K.P.; 1990, "A Review of Reaction Rates and Thermodynamic and Transport Properties for an 11-Species Air Model for Chemical and Thermal Non-equilibrium Calculations to 30000 K," NASA Reference Publication, No. 1232.

[74] Davidenko D.M., Gökalp I., Dufour E. & Magre P.; 2006, "Systematic Numerical Study of the Supersonic Combustion in an Experimental Combustion Chamber", AIAA Paper 06-7915.

[75] Ben-Yakar A., Mungal M.G. & Hansen R.K.; 2006, "Time Evolution and Mixing Characteristics of Hydrogen and Ethylene Transverse Jets in Supersonic Crossflows", **18**, p 026101.

[76] Bowen J.R. (Ed.); 1992, "Dynamics of Exothermicity", Gordon and Breach Publishers, p. 292.

[77] Kuhl A.L., Fergusson R.E. & Oppenheim A.K.;1963, " Gasdynamic Model of Turbulent Exothermic Fields in Explosions ", Progress in Astronautics and Aeronautics, **173**, p. 251.

[78] Ingignoli W.; 1999, "Etude de la formation et de la propagation des detonations dans des suspensions de particules d'aluminium en atmosphere oxydante ou reactive", PhD Thesis, Université de Poitiers.

[79] Fedina E., Fureby C. & Helte A.; 2010, "Predicting Mixing and Combustion in the Afterburn Stage of Air Blasts", AIAA-2010-0773.

[80] Taylor G.I.; 1950, "The Instability of Liquid Surfaces when Accelerated in a Direction Perpendicular to their Planes", Proc. of Royal Society of London. Series A, **201**, p.192.

[81] Richtmyer R.D.; 1960, "Taylor Instability in a Shock Acceleration of Compressible Fluids", Com. Pure and Appl. Math., **13**, p. 297.

[82] Gui M., Fan B., Dong G. & Ye J.; 2009, "Interaction of a Reflected Shock from a Concave Wall with Flame Distorted by an Incident Shock", Shock Waves, **18**, p. 487.

[83] CONWEP – Conventional Weapons; 1992, Collection of Conventional Weapons Calculations based on T-5-855-1, Fundamentals of Protective Design for Conventional Weapons.

[84] Almström H.; 2003, "Registration and Simulation of Air Blast Pressure of a Detonation Charge Above Ground", Methodology Report, no FOI-R-0819—SE, Swedish Defense Research Agency, Weapons and Protection Division.

[85] Baker W.E.; 1973, "Explosions in Air", University of Texas Press.